AIAA JOURNAL
Vol. 46, No. 6, June 2008

Parametric Study of an Oscillating Airfoil in a Power-Extraction Regime

T. Kinsey* and G. Dumas†
Université Laval, Québec City, Québec G1K 7P4, Canada

DOI: 10.2514/1.26253

A wing that is heaving and pitching simultaneously may extract energy from an oncoming flow, thus acting as a turbine. The theoretical performance of such a concept is investigated here through unsteady two-dimensional laminar-flow simulations using the commercial finite volume computational fluid dynamics code FLUENT. Computations are performed in the heaving reference frame of the airfoil, thus leaving only the pitching motion of the airfoil to be dealt with through a rigid-body mesh rotation and a circular nonconformal sliding interface. Unsteady aerodynamics basics of the oscillating airfoil are first exposed, with a description of the operating regimes. Effects of unsteadiness are stressed and the inadequacy of a quasi-steady approach to take them into account is exposed. We present a mapping of power-extraction efficiency for a single oscillating airfoil in the frequency and pitching-amplitude domain: $0 < fc/U_\infty < 0.25$ and $0 < \theta_0 < 90\,\mathrm{deg}$ for a NACA 0015 airfoil at a Reynolds number of $Re = 1100$, a heaving amplitude of one chord ($H_0 = c$), and a pitching axis at the third chord ($x_p = c/3$). Remarkably, efficiency as high as 34% is observed, as well as a large parametric region at $\theta_0 > 55\,\mathrm{deg}$ in which efficiencies are higher than 20%. Results from a parametric study are then provided and discussed. It is found that motion-related parameters such as heaving amplitude and frequency have the strongest effects on airfoil performances, whereas geometry and viscous parameters turn out to play a secondary role.

Nomenclature

C	=	nondimensional coefficient
c	=	chord length
D	=	drag force defined with respect to the instantaneous effective flow direction
d	=	overall vertical displacement
f	=	frequency of oscillation of period T, $1/T$
f^*	=	nondimensional frequency, fc/U_∞
H_0	=	heaving amplitude
h	=	instantaneous vertical position of the airfoil pitching axis
L	=	lift force defined with respect to the instantaneous effective flow direction
M	=	torque about x_p
P	=	instantaneous total power extracted, $P_y + P_\theta$
P_a	=	total power available, $\frac{1}{2}\rho U_\infty^3 d$
P_y	=	heaving contribution to instantaneous total power, YV_y
P_θ	=	pitching contribution to instantaneous total power, $M\Omega$
p	=	pressure on the airfoil
R	=	resultant aerodynamic force
Re	=	Reynolds number, $U_\infty c/\nu$
U_∞	=	freestream velocity
V_{eff}	=	effective upstream velocity, $\sqrt{U_\infty^2 + V_y^2}$
V_y	=	instantaneous heaving velocity
V_R	=	peak velocity ratio, $V_{y\max}/U_\infty = 2\pi f^* H_0/c$
X	=	horizontal component of aerodynamic force
x_p	=	chordwise position of pitching axis
Y	=	vertical component of aerodynamic force
α	=	effective angle of attack, $\arctan(-V_y/U_\infty) - \theta$
$\alpha_{T/4}$	=	quarter-period effective angle of attack ($\lvert\alpha_{T/4}\rvert \approx \alpha_{\max}$), $\arctan(V_R) - \theta_0$
γ	=	angular frequency, $2\pi f$
η	=	efficiency, $\bar{P}/P_a$
θ	=	instantaneous angular position of the airfoil chord w/r to horizontal
θ_0	=	pitching amplitude
Φ	=	cylinder diameter
ϕ	=	phase shift between pitching and heaving motions
χ	=	feathering parameter, $\theta_0/\arctan(H_0\gamma/U_\infty)$
Ω	=	pitching angular velocity
$\bar{}$	=	mean value over one motion cycle (cycle-averaged quantity)
$\hat{}$	=	peak value over one motion cycle

Presented as Paper 2836 at the 24th AIAA Applied Aerodynamics Conference, San Francisco CA, 5–8 June 2006; received 24 July 2006; revision received 17 August 2007; accepted for publication 5 February 2008. Copyright © 2008 by T. Kinsey and G. Dumas. Published by the American Institute of Aeronautics and Astronautics, Inc., with permission. Copies of this paper may be made for personal or internal use, on condition that the copier pay the $10.00 per-copy fee to the Copyright Clearance Center, Inc., 222 Rosewood Drive, Danvers, MA 01923; include the code 0001-1452/08 $10.00 in correspondence with the CCC.

*Ph.D. Student, Laboratoire de Mécanique des Fluides Numérique, Département de Génie Mécanique; thomas.kinsey.1@ulaval.ca.

†Professor, Laboratoire de Mécanique des Fluides Numérique, Département de Génie Mécanique; gdumas@gmc.ulaval.ca.

I. Introduction

THE recent rise of fuel prices and the growing commitment of the international community to limit greenhouse effect motivate the development of alternative power-generation systems from renewable sources. One promising concept in the fields of wind turbines and tidal energy systems relies on the use of oscillating wings, simultaneously heaving and pitching, as power-extraction devices. This concept was initially proposed by McKinney and DeLaurier [1] in 1981 and was further investigated by Jones et al. [2] more recently.

The present investigation on oscillating airfoils is based on unsteady laminar 2-D numerical simulations of the complex viscous flows resulting when large-amplitude motions are considered. We restrict this work to laminar-flow conditions at Reynolds numbers of $\mathcal{O}(10^3)$ (except in Sec. IV.B.3) to avoid introducing uncertainties associated with turbulence modeling and to keep computing costs reasonable, allowing a great number of cases to run. This study thus aims to determine the optimal aerodynamic parameters maximizing the efficiency of power extraction achieved by a single airfoil at low Reynolds numbers. The new data and physical insights provided in this work should stimulate further investigations and help to guide the design and testing of actual power-extraction systems based on the oscillating-wing concept.

In this paper, we first present a description of the aerodynamics of oscillating airfoils with proper characteristics of each operating regime: namely, power extraction and propulsion. The inadequacy of a quasi-steady approximation for the flow about an oscillating airfoil

was addressed by Theodorsen [3] in his classical work on unsteady aerodynamics and aeroelasticity. The present investigation confirms this inadequacy, extending the study to the strong nonlinear situations of viscous flows and large amplitudes of motion. It is found that unsteadiness is responsible for considerably higher instantaneous force coefficients, which represents an attractive characteristic for the development of higher-performance turbines or propulsion devices.

A mapping of power-extraction efficiency in the parametric space (f^*, θ_0) (the frequency/pitching-amplitude space) is then presented for a given airfoil geometry, a fixed Reynolds number, a fixed heaving amplitude, and a given pitching-axis location. Furthermore, the impact of varying the previously fixed parameters is discussed, and their relative importance is emphasized.

Numerical simulations in this work are performed with an Eulerian approach using an innovative dynamic mesh strategy. Accuracy of the numerical predictions presented here is well ascertained through a thorough validation process that involves rigorous spatial and temporal convergence tests as well as comparisons with independent numerical simulations carried out with an in-house Lagrangian-vortex-method solver.

II. Oscillating-Airfoil Basics

A. Motion Description

We define an oscillating wing as an airfoil experiencing simultaneous pitching $\theta(t)$ and heaving $h(t)$ motions, as shown in Fig. 1. Restricting to a pitching axis located on the chord line at position x_p from the leading edge, the airfoil motion is expressed as

$$\theta(t) = \theta_0 \sin(\gamma t) \rightarrow \Omega(t) = \theta_0 \gamma \cos(\gamma t) \tag{1}$$

$$h(t) = H_0 \sin(\gamma t + \phi) \rightarrow V_y(t) = H_0 \gamma \cos(\gamma t + \phi) \tag{2}$$

where θ_0 and H_0 are, respectively, the pitching and heaving amplitudes; Ω is the pitching velocity; V_y is the heaving velocity; γ is the angular frequency $(2\pi f)$; and ϕ is the phase difference between the two motions. In the current study, only symmetric airfoils are considered, and ϕ is kept constant at 90 deg. The freestream velocity far upstream of the oscillating airfoil is U_∞.

B. Operating Regimes

One must know that an oscillating symmetric airfoil can operate in two different regimes: namely, propulsion and power extraction. This fundamental distinction originates from the sign of the forces that the flow generates on the moving airfoil. Based on the motion imposed and upstream flow conditions, the airfoil experiences an effective angle of attack α and an effective upstream velocity V_{eff}, obviously functions of time, expressed as follows:

$$\alpha(t) = \arctan(-V_y(t)/U_\infty) - \theta(t) \tag{3}$$

$$V_{\text{eff}}(t) = \sqrt{U_\infty^2 + V_y(t)^2} \tag{4}$$

Their maximum values in the cycle are expected to have a major impact on the peak forces generated and on the possibility of dynamic-stall occurrence. The maximum effective angle of attack reached in one cycle is approximated by the modulus of its quarter-period value (exact approximation in most cases):

$$\alpha_{\max} \approx |\alpha_{T/4}| = |\arctan(\gamma H_0/U_\infty) - \theta_0| \tag{5}$$

The maximum effective velocity also occurs at the quarter-period:

$$V_{\max} = V_{\text{eff}}(T/4) = \sqrt{U_\infty^2 + (\gamma H_0)^2} \tag{6}$$

To qualify the effect of the imposed motion on the flow regime, one defines a *feathering parameter* [4] as

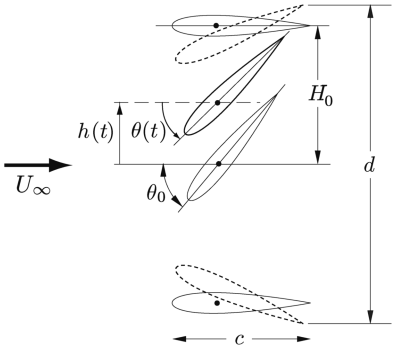

Fig. 1 Imposed heaving and pitching motions ($\phi = 90$ deg).

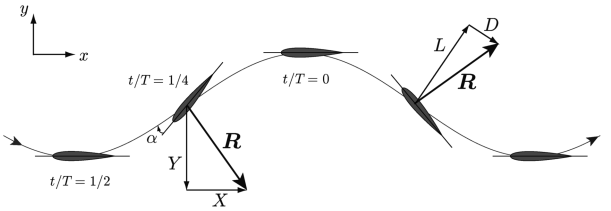

Fig. 2 Power-extraction regime ($\chi > 1$ and $\alpha_{T/4} < 0$) of an oscillating airfoil viewed in the freestream velocity reference frame; apparent motion of the airfoil is from right to left and effective velocity vector coincides with the apparent trajectory.

$$\chi = \frac{\theta_0}{\arctan(H_0\gamma/U_\infty)} \tag{7}$$

Based on a simple quasi-steady argument, which leads to necessary, but not precisely sufficient, conditions (in a mean sense over the cycle), one can show that $\chi < 1$ is associated with propulsion ($\alpha_{T/4} > 0$), whereas $\chi > 1$ corresponds to power extraction ($\alpha_{T/4} < 0$). An example of the latter case is shown in the schematic representation of Fig. 2, which presents a time sequence viewed in a reference frame moving with the far-field flow at U_∞, so that the effective angle of attack $\alpha(t)$ is made visible from the apparent trajectory of the airfoil. In that figure, the resultant force **R** is first constructed from typical lift and drag forces (right-hand side) and then decomposed into X and Y components (left-hand side). One easily infers in Fig. 2 that the resultant aerodynamic force **R** would have a vertical component Y that is in the same direction as the vertical displacement of the airfoil. The flow would thus make a positive work on the airfoil, and therefore power would be extracted as long as no negative work is involved with respect to the horizontal component X. This is precisely the case of interest here, because our airfoil is actually not moving horizontally, but only pitching and heaving into a uniform flow from left to right at speed U_∞.

The particular case $\chi = 1$ shown in Fig. 3a implies that the resultant force **R** is tangent and opposed to the motion of the airfoil (no lift, only drag under the quasi-steady assumption). However, this is actually the case only when $\alpha(t) = 0$ in the cycle, which happens at every quarter-period ($t = iT/4$, $i = 0, 1, 2, \ldots$) under the sole condition $\chi = 1$ [as depicted in Fig. 3b from the $\alpha(t)$ curve]. This particular situation is hereafter referred to as the *feathering limit*. To guarantee that the effective angle of attack α is kept null over the whole cycle, one must modify the pitching function Eq. (1) as

$$\theta(t) = \arctan\left(\frac{-V_y(t)}{U_\infty}\right) \tag{8}$$

This is the special-case scenario we refer to as the *feathering regime*.

Finally, in the schematic of Fig. 4, one observes that the motion of the airfoil may produce a horizontal force X toward the left, thus resulting in a net propulsion. Of course, this propulsion is achieved at the price of doing some work on the fluid through Y opposing the vertical displacement of the airfoil.

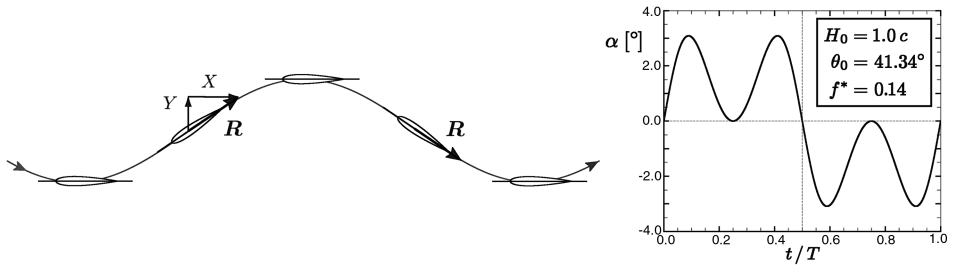

a) b)

Fig. 3 Feathering regime ($\chi = 1$ and $\alpha_{T/4} = 0$) of an oscillating airfoil: a) schematic and b) corresponding effective angle-of-attack evolution [Eq. (3)] over one periodic cycle.

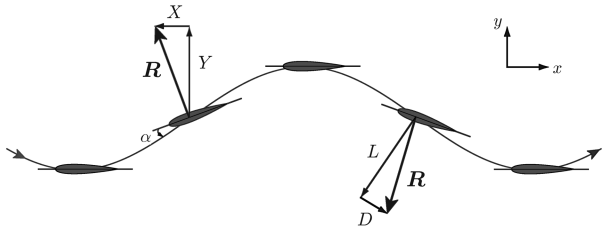

Fig. 4 Propulsion regime ($\chi < 1$ and $\alpha_{T/4} > 0$) of an oscillating airfoil.

For analysis purposes, it is convenient to consider the parametric space (f^*, θ_0) (see Fig. 5), which is divided in two zones by the curve corresponding to the feathering limit. The power-extraction area falls above this limit, whereas cases below it belong to the propulsion regime.

It thus clearly appears that one may change the operating regime of an airfoil oscillating at a given frequency simply by varying its pitching amplitude, thus affecting $\alpha_{T/4}$ and χ. Once again, note the necessary, but not sufficient, character of the condition of being on one side or the other of the feathering limit to actually achieve propulsion or power extraction in a mean sense over the cycle.

Figure 5 also presents isolines of $|\alpha_{T/4}|$ plotted parallel to the feathering limit, which is itself the curve corresponding to $\alpha_{T/4} = 0$ deg. Although effective angles of attack as high as 40 deg would be considered irrelevant in a steady aerodynamic perspective, such high values are considered in Sec. IV for their possible benefits due to dynamic-stall vortex shedding.

Examples of typical X and Y force-coefficient evolutions over one periodic cycle are also provided in Fig. 5 for each operating regime. For reference, the heaving velocity V_y is also plotted. For the power-extraction case, the positive cycle-averaged product $C_Y(t) \cdot V_y(t)/U_\infty$ implies net power extracted, whereas $\bar{C}_X > 0$ indicates a net drag over the cycle. For the propulsion case, the horizontal force component evolution leads to $\bar{C}_X < 0$, indicating a net propulsion over the cycle. The work needed to propulse the airfoil is primarily given by the cycle-averaged product $C_Y(t) \cdot V_y(t)/U_\infty$, which is therefore negative here.

C. Wake Signature

Obviously, oscillating airfoils tend to produce counter-rotating vortices in their wakes. It is often possible to identify which regime a given case belongs to just by looking at its wake.

In the power-extraction regime, one always gets a positive mean $\bar{C}_X$ over one cycle (e.g., Fig. 5, top). As shown in Fig. 6a, the wake in such cases takes the form of a drag-producing Karman-like vortex street. The velocity induced by the wake vortices (more precisely, the x component) is consistent with the expected x velocity deficit near the center of a dragging body.

On the other hand, in the airfoil reference frame, propulsion cases such as that shown in Fig. 6b should present a pattern of vortices that induces, in the mean, a positive x component of velocity. One might refer to it as a jetlike pattern, consistent with the net thrust of a self-propelled body.

Considering the mean velocity profiles in these wakes, one can thus infer that at the same oscillation frequency, the vortices generated in the propulsion regime should be convected away from the airfoil faster than vortices produced in the power-extraction regime.

D. Extracted Power and Efficiency

The instantaneous power extracted from the flow (per unit depth) when $\chi > 1$ comes from the sum of a heaving contribution $P_y(t) = Y(t)V_y(t)$ and a pitching contribution $P_\theta(t) = M(t)\Omega(t)$, where M is the resulting torque about the pitching center x_p. The mean power extracted over one cycle can thus be computed in nondimensional form:

$$C_P \equiv \frac{P}{\frac{1}{2}\rho U_\infty^3 c}$$

as

$$\bar{C}_P = \bar{C}_{P_y} + \bar{C}_{P_\theta} = \int_0^1 \left\{ C_Y(t)\frac{V_y(t)}{U_\infty} + C_M(t)\frac{\Omega(t)c}{U_\infty} \right\} \mathrm{d}(t/T) \tag{9}$$

We further define the power-extraction efficiency η as the ratio of the mean total power extracted $\bar{P}$ to the total power available P_a in the oncoming flow passing through the swept area (the flow window):

$$\eta \equiv \frac{\bar{P}}{P_a} = \frac{\bar{P}_y + \bar{P}_\theta}{\frac{1}{2}\rho U_\infty^3 d} = \bar{C}_P \frac{c}{d} \tag{10}$$

where d is the overall vertical extent of the airfoil motion. This distance considers both heaving and pitching motions, as shown in Fig. 1, and is typically slightly larger than $2H_0$. The power-extraction efficiency is theoretically limited to 59% from the Betz [5] analysis of a stationary inviscid stream tube around a power-extraction device.

III. Numerics

A. Unsteady and Viscous Effects

The aerodynamics of a moving body are far more complex than the aerodynamics of a steady body. In a first attempt to model the former, it could be tempting to use instantaneous force coefficients from stationary data matching the instantaneous angle of attack. However, such a quasi-steady hypothesis lacks the effect of history inherent to unsteady problems and fails to predict accurate results even for smooth cases far away from dynamic stall.

To illustrate the strong limitations of the quasi-steady approach, preliminary calculations of true feathering {feathering regime $\alpha(t) = 0$ [Eq. (8)]} were computed for different frequencies. Evolutions of lift coefficient over one periodic cycle are shown in Fig. 7, in which a quasi-steady hypothesis would predict no lift at all ($C_L(t) = 0$). It is clearly seen that unsteady effects are significant (C_L reaching up to 0.5 for a frequency $f^* = 0.14$) and grow with frequency as expected. Some unsteady wake interaction is visible on the vorticity field associated with $f^* = 0.14$.

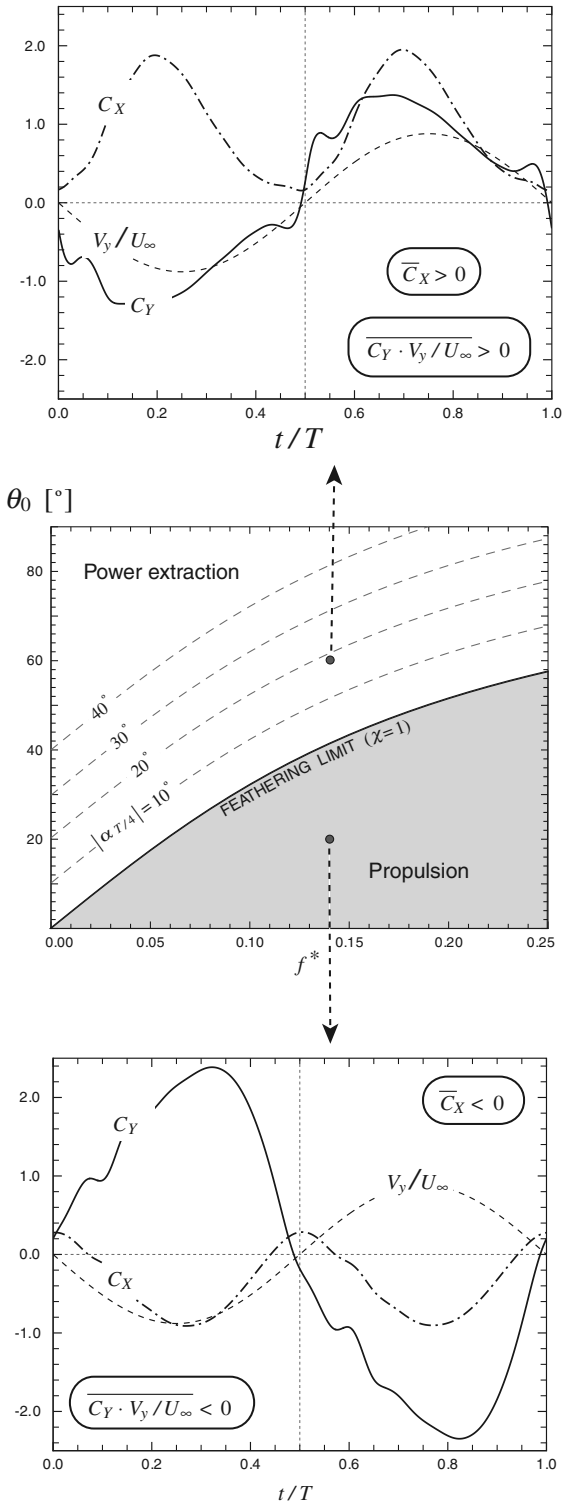

Fig. 5 Operating regimes in (f^*, θ_0) parametric space with isolines of maximum effective angle of attack ($\alpha_{max} \approx |\alpha_{T/4}|$); typical force coefficients C_X and C_Y along with heaving velocity V_y/U_∞ are provided over one periodic cycle for a power-extraction case (top) and a propulsion case (bottom).

Modeling of the unsteady flows about moving bodies with inviscid aerodynamic approaches, such as panel methods, would thus improve matters. However, inviscid approaches are limited to cases experiencing no dynamic stall [2]. This limitation is seriously restrictive, because dynamic stall plays a key role in oscillating-airfoil performance, as will be discussed in Sec. IV. In this study, we therefore rely on a more computational intensive method: namely, on an unsteady Navier–Stokes solver.

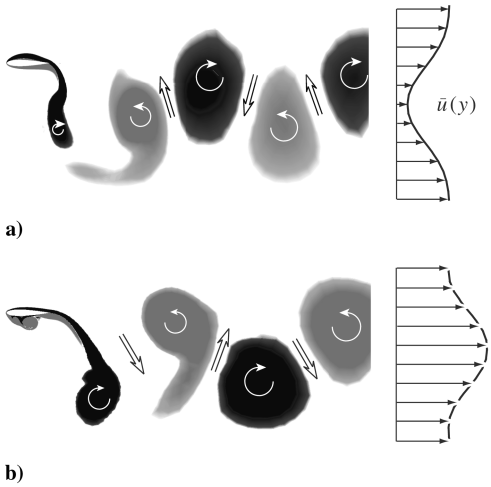

Fig. 6 Instantaneous vorticity field with directions of wake-vortice-induced velocities for a) a typical power-extraction case ($f^* = 0.22$), and b) a typical propulsion case ($f^* = 0.35$); mean x velocity profiles are also sketched.

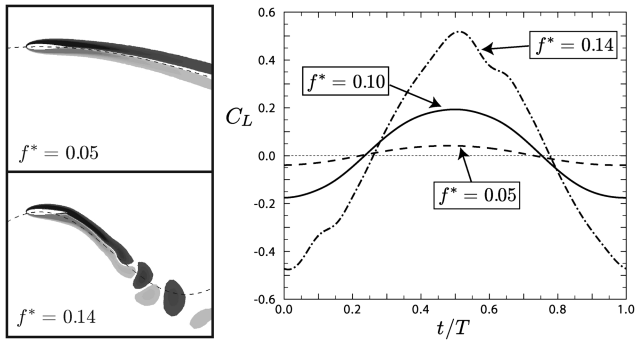

Fig. 7 Unsteady effects in feathering-mode cases with $\alpha(t) = 0$ [see Eq. (8)]; NACA 0015; $Re = 1100$: a) vorticity fields at $t/T = 0$ with the airfoil path line added for reference (gray for positive ω and black for negative) and b) instantaneous lift; $C_L(t) = 0$ would be predicted under quasi-steady hypothesis.

B. Flow Solver

High resolution two-dimensional unsteady computations are performed in this study at Reynolds numbers from 500 to 10,000 with the commercial finite volume code FLUENT 6.1 [6]. A second-order-accurate upwind scheme is used to discretize convection terms, and diffusion-term discretization is done with the second-order central-differencing scheme. A second-order-accurate backward-implicit scheme is used to discretize time. A pointwise Gauss–Seidel linear equation solver is used to solve the discretized equations, in conjunction with an algebraic multigrid method accelerating convergence. The velocity-pressure coupling is based on a semi-implicit method for pressure-linked equations (SIMPLE) segregated algorithm.

C. Dynamic Mesh Strategy

Because FLUENT allows for the use of moving meshes, the straightforward strategy would be to consider an inertial (fixed) reference frame. Both heaving and pitching motions of the airfoil would then be taken into account through mesh motion and regular remeshing. However, this approach in FLUENT requires the use of first-order time integration, which therefore imposes the use of very small time-step sizes to control the inherent numerical diffusion.

To circumvent this constraint, a different meshing strategy was developed in this work. In the present approach, the problem is set in a heaving reference frame (vertical translation) attached to the airfoil. The pitching portion of the airfoil motion is left as such; that is, the airfoil is actually rotating in the translating reference frame. This implies the use of time-varying velocity conditions on the inflow domain boundary and the addition of a new source term in the

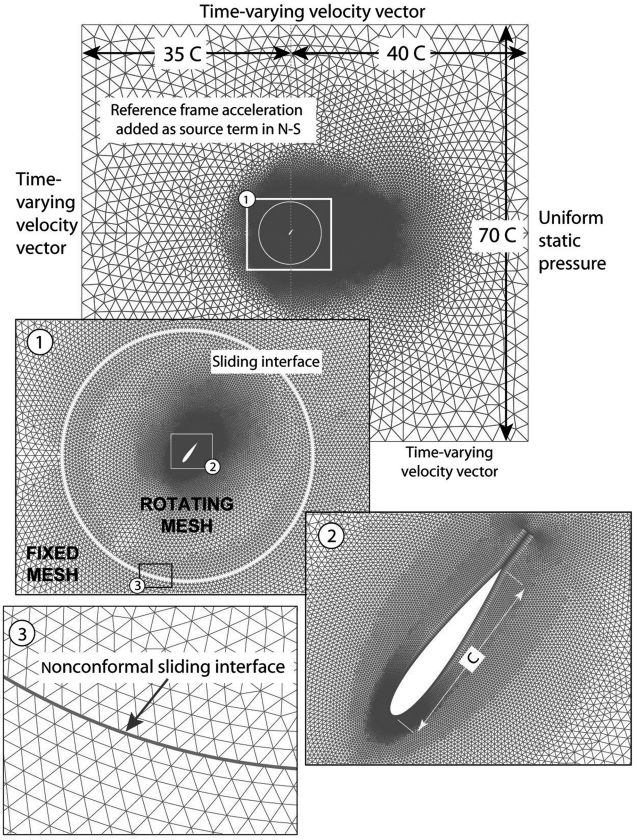

Fig. 8 Grid details with two zoom levels showing its circular nonconformal, sliding interface; typical grid size is 72,000 cells and near-body resolution is $Re_\Delta = \omega \Delta^2 / \nu = \mathcal{O}(1)$.

Navier–Stokes equation to account for the reference-frame acceleration. Hence, mesh motion is necessary only for the rotating (pitching) motion of the airfoil. This is done by splitting the calculation domain into two zones bounded by a circular nonconformal sliding interface. As can be seen in Fig. 8, this interface is located at five chords around the airfoil, and the grid inside is pitching in rigid-body motion with the airfoil. The grid outside the interface is not moving. This strategy offers the significant advantage of allowing for the use of second-order time-integration scheme, rather than only first-order when solving in a fixed inertial reference frame.

To reach the long-term periodic-flow response after the impulsive start in each of our simulations, a few cycles are first computed with a relaxed time-step size. The precise number of cycles computed at that stage depends on the period of oscillation $T = 1/f$. This transitory period should provide at least 20 convective time units (i.e., time enough for the early wake to get sufficiently far away from the body). From that point on, calculation is pursued using a finer time resolution given by

$$\Delta t = \min\left\{\frac{T}{2000}; \frac{c/\|V\|}{100}\right\} \tag{11}$$

where $\|V\|$ is a velocity norm representing the maximum instantaneous convective flux velocity in the domain, which takes into account U_∞, the heaving boundary condition, and the pitching mesh velocity. Normalized flow diagnostics are thereafter monitored to ascertain the periodicity of the final cycles. A criterion of less than 0.1% variation in mean statistics between final cycles is typically used. Flow quantities and aerodynamic forces of the last cycle are then recorded and used to compute various mean values as well as the power-extraction efficiency. The typical run time for a whole simulation is about 100 h on a single P4/3.2-GHz processor.

D. Validation

To validate our numerical predictions, rigorous self-consistency tests were carried out to assure satisfactory independency of the force predictions with respect to both mesh and time discretizations. Unfortunately, there are yet no experimental data available for low-Reynolds-number oscillating airfoils in a power-extraction regime. Therefore, to further support our numerical predictions, we adapted an in-house Lagrangian-vortex-method solver provided to us by Ploumhans and Winckelmans [7] to independently recompute several of the Eulerian simulations. Some of this validation effort is presented in this paper.

First, the case of a cylinder undergoing vertical sinusoidal oscillation was used to test our simulation approach with respect to our choice of working in the heaving reference frame. This flow was computed at the Reynolds number of 500 with a high-accuracy spectral element method by Blackburn and Henderson [8]. Excellent agreement on instantaneous and mean force predictions was achieved for both levels of resolution tested, as shown in Table 1.

The complete strategy involving the use of a sliding nonconformal interface to allow rigid-body rotation of a circular mesh zone adjacent to the body was validated through comparisons with high-accuracy oscillating-airfoil results produced with the in-house Lagrangian-vortex-particles method [7,9], which, in essence, is a mesh-free-solution method. Thus, by nature, both solvers (the Eulerian and the Lagrangian) are completely different and independent. Results of instantaneous forces and moments over time for a periodic cycle are found to be in excellent agreement, as shown in Fig. 9 for a typical case (referred to as case 1) of high-efficiency power extraction. This agreement strongly supports our overall numerical strategy as well as the resolution level used in our production runs, as discussed next.

Autovalidation tests were also systematically performed for three different, physically significant, operating points in the parametric space of reduced frequency and pitching amplitude. Cases 1 and 3 involve strong dynamic-stall and leading-edge vortex shedding (LEVS), but at quite different frequencies, whereas case 2 (at the highest frequency) is much smoother and only exhibits boundary layers at the onset of dynamic stall. Results for space and time refinements are shown in Table 2.

Three different mesh resolutions were used: a coarse mesh (16,000 cells and 140 nodes on the airfoil), a medium mesh (72,000 cells and 280 nodes on the airfoil), and a fine mesh (253,000 cells and 560 nodes on the airfoil). To establish time-discretization independency, three levels of time steps per cycle were also considered (using the medium mesh): 500, 2000, and 4000. It can be seen from Table 2 that for all three cases, 2000 time steps per cycle yields time-accurate predictions for both mean and instantaneous values. Furthermore, results show that our medium-mesh resolution provides satisfactory accuracy in space, as far as force and efficiency predictions are concerned. Indeed, for our three test cases, differences between medium- and fine-mesh results are quite small, with variations of less

Table 1 Comparison of mean horizontal force coefficient and peak vertical force coefficient with the spectral element method predictions of Blackburn and Henderson [8] for a heaving cylinder; $Re = U_\infty \Phi/\nu = 500$, $f^* = f\Phi/U_\infty = 0.228$, and $H_0/\Phi = 0.25$

Solver	Cells	Time steps/cycle	$\bar{C}_X$	$\hat{C}_Y$
Present (coarse)	38,800	2000	1.397	1.729
Present (medium)	65,600	2000	1.412	1.755
Blackburn and Henderson[8]	422 (ninth order)	2000	1.414	1.776

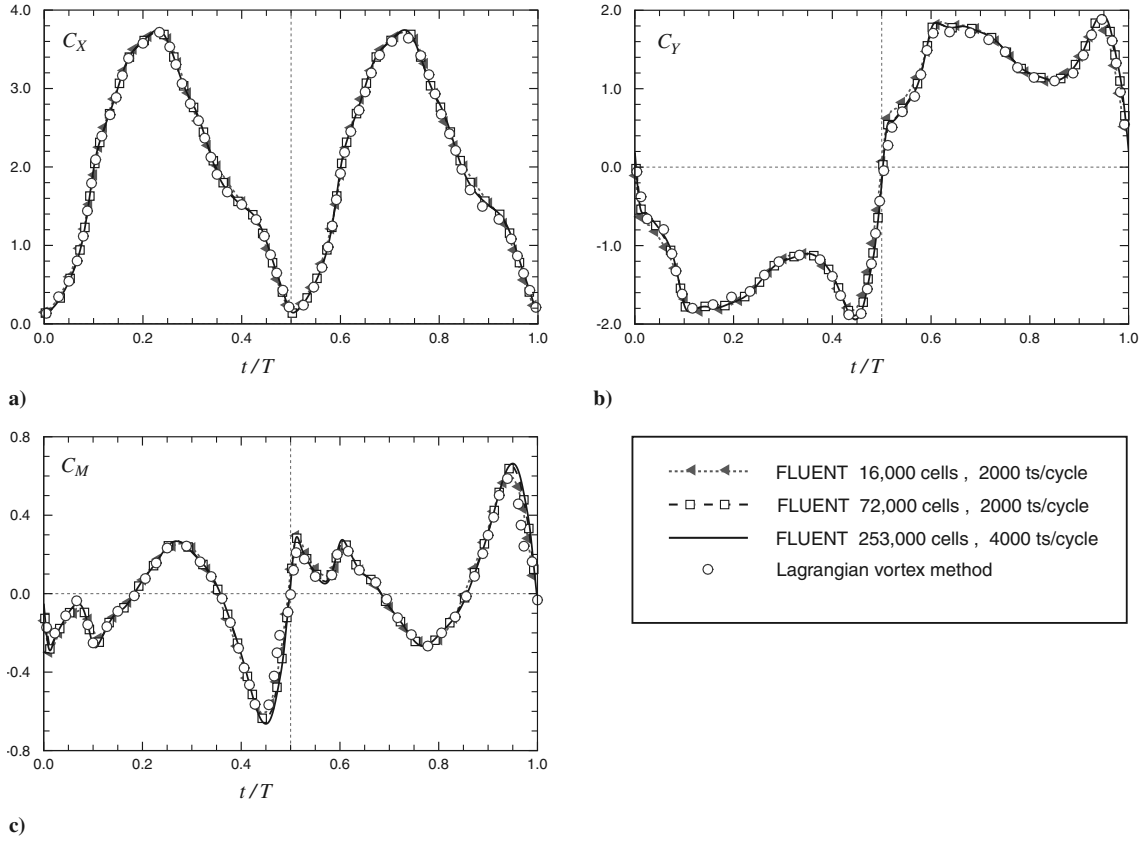

Fig. 9 ***X*** **and** ***Y*** **forces and pitching moment** ***M*** **(at third chord) coefficients over time for a periodic cycle; for clarity, only 3% of the data symbols are plotted; NACA 0015;** $Re = 1100$, $H_0/c = 1$, $f^* = 0.14$, $\theta_0 = 76.33\,\text{deg}$, **and** $x_p/c = 1/3$.

than 3% on instantaneous peak force coefficients, whereas cycle-averaged values (such as mean C_X and efficiency) closely match within 1%.

Instantaneous pressure-coefficient distributions at two different times in the airfoil motion cycle of case 1 are also provided in Fig. 10 to demonstrate the accuracy of the medium-mesh resolution on the instantaneous flowfield near the body. Once again, the very good agreement between medium- and fine-discretization results led us to adopt the 72,000-cell mesh and 2000 time steps per cycle as the standard for our production runs. Note, however, that the number of time steps per cycle was slightly increased above 2000, in accordance with Eq. (11), for a few particular cases (included in the mapping of Fig. 11) for which very low frequency or faster airfoil motion yielded a dominant convective criterion.

IV. Results of the Power-Extraction Performance

A. Efficiency of the Basic Set of Parameters

To identify interesting operating zones, all parameters were initially kept fixed, except for frequency and pitching amplitude. This group of fixed parameters constitutes our basic configuration: NACA 0015 airfoil, $Re = U_\infty c/\nu = 1100$, $H_0/c = 1$, and

Table 2 Results of validation through space and time refinements for an airfoil in power-extraction regime; NACA 0015; $Re = 1100$, $H_0/c = 1$, **and** $x_p/c = 1/3$

Validation	Cells	Time steps/cycle	$\bar{C}_X$	$\hat{C}_Y$	$\hat{C}_M$	η, %
		Case 1: $f^* = 0.14$ and $\theta_0 = 76.33$ deg				
Time	72,000	500	2.011	1.882	0.635	33.6
	72,000	2000	2.014	1.910	0.646	33.7
	72,000	4000	2.014	1.909	0.645	33.7
Space	16,000	2000	2.027	1.857	0.612	33.6
	72,000	2000	2.014	1.910	0.646	33.7
	253,000	4000	2.019	1.942	0.664	33.9
		Case 2: $f^* = 0.18$ and $\theta_0 = 60.0$ deg				
Time	72,000	500	0.688	1.254	0.298	11.4
	72,000	2000	0.690	1.256	0.299	11.4
	72,000	4000	0.690	1.256	0.299	11.4
Space	16,000	2000	0.683	1.262	0.304	11.0
	72,000	2000	0.690	1.256	0.299	11.4
	253,000	4000	0.692	1.254	0.298	11.5
		Case 3: $f^* = 0.06$ and $\theta_0 = 60.0$ deg				
Time	72,000	500	1.264	2.045	0.598	12.3
	72,000	2000	1.256	2.030	0.597	12.3
	72,000	4000	1.255	2.029	0.597	12.3
Space	16,000	2000	1.251	2.042	0.597	12.0
	72,000	2000	1.256	2.030	0.597	12.3
	25,300	4000	1.257	2.032	0.594	12.3

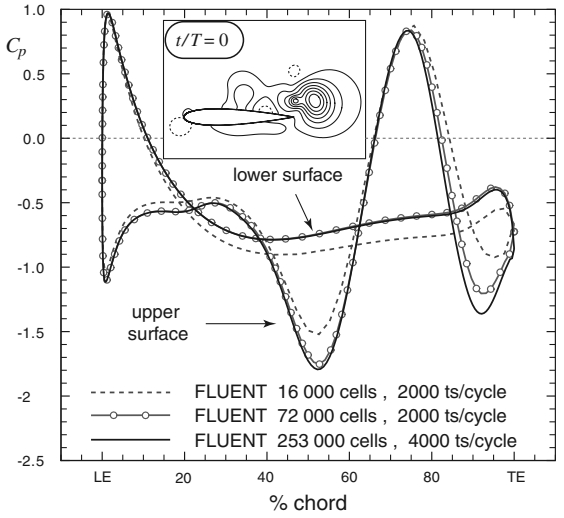

a)

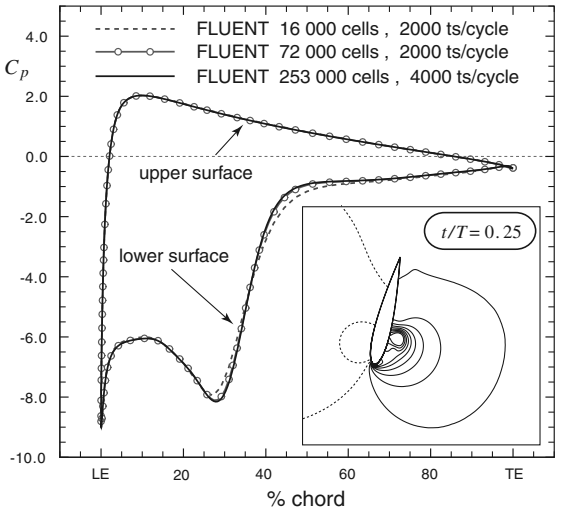

b)

Fig. 10 Pressure-coefficient distribution from the leading edge to the trailing edge at a) $t/T = 0$ and b) $t/T = 0.25$; corresponding contours of pressure are also provided (dashed for positive; solid for negative); NACA 0015; $Re = 1100$, $H_0/c = 1$, $f^* = 0.14$, $\theta_0 = 76.33$ deg, and $x_p/c = 1/3$.

$x_p/c = 1/3$. A mapping of the predicted efficiencies (nearly 50 simulations) in the parametric space (f^*, θ_0) is provided in Fig. 11 for the basic set of parameters. Note that the dimensionless frequency is defined here as $f^* \equiv fc/U_\infty$.

First, we find that the highest efficiency achieved ($\eta_{\max} \approx 34\%$) is obtained for high pitching amplitudes ($\theta_0 \approx 70$–80 deg) and at nondimensional frequencies in the range of $f^* \approx 0.12$–0.18. As a reference, let us recall the theoretical limit of Betz [5] (from actuator disk theory) at 59%, which should apply to the present oscillating-wing problem because a cycle-averaged stationary flow concept may be defined. In any case, efficiencies higher than 30% for a single oscillating airfoil appear quite encouraging from a practical point of view for the present turbine concept.

We further note that the best-efficiency cases in Fig. 11 correspond to operating conditions of roughly $f^* = 0.15$, which yields

$$V_{y\max}/U_\infty = 2\pi f^* H_0/c \approx 1$$

(maximum heaving velocity, comparable with the freestream velocity). At the same time, these cases are found to involve effective angles of attack [see Eq. (3) and the isolines of $|\alpha_{T/4}|$ in Fig. 11] reaching as high as 35 deg during their cycles. With such large values of angle of attack, it is no surprise to observe some dynamic-stall

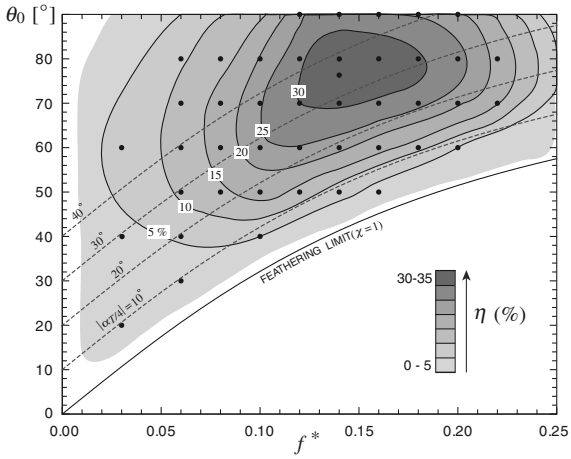

Fig. 11 Mapping of efficiency η in the parametric space (f^*, θ_0) for a NACA 0015 at $Re = 1100$, $H_0/c = 1$, and $x_p/c = 1/3$; simulated cases are shown with black dots and isoefficiency contours are sketched approximately.

vortex shedding taking place during the motion. Although boundary-layer separation leads to unfavorable effects in stationary aerodynamics, dynamic-stall vortex shedding is found to contribute toward increased performances. Indeed, LEVS is seen to occur during the cycles of most of the efficient cases (see Fig. 12). In fact, one finds that well-timed LEVS, occurring each half-period just before $t \approx 0$ and $T/2$, is a very important mechanism to maximize the power-extraction efficiency, as can be illustrated with the help of Fig. 12.

Case 1 (shown in Fig. 12a) exhibits dynamic-stall vortex shedding and reaches a mean efficiency of nearly 34%, whereas case 2 (shown in Fig. 12b), which is at a slightly higher frequency and lower pitching amplitude, corresponds to a typically smooth aerodynamic flow with a moderate efficiency of $\eta = 11\%$. Note that a straight horizontal line corresponding to the theoretically available power C_{P_a} was added to the figures as a reference level.

The main feature revealed by Fig. 12 is that case 2 (Fig. 12b), without LEVS, shows a poor synchronization between the heaving velocity V_y and the vertical force coefficient C_Y (i.e., they have opposite signs at times), causing the total power curve C_P to go negative in some parts. On the other hand, case 1 (Fig. 12a), exhibiting dynamic stall, shows good timing in the sign switch of V_y and C_Y, resulting in positive values of total extracted power over almost all of the cycle. It is clearly the shed vortices and their suction effect on the airfoil (see pressure contours) that are responsible for maintaining a negative Y force much closer to the midcycle time at $t/T = 0.5$.

In this particular case, one notes further that the shedding at each half-cycle has also a favorable impact on the pitching contribution P_θ, which can play a positive role momentarily in the cycle, despite its small overall mean contribution.

Indeed, one finds in this study that for most cases of interest (and $f^* \leq 0.16$), the heaving contribution P_y to the total power extracted significantly dominates the pitching contribution P_θ. One may thus assume $P(t) \approx Y(t)V_y(t)$ for most analysis purposes. Consequently, we find that there are three major aspects affecting the level of power extracted: 1) synchronization of $Y(t)$ and $V_y(t)$, 2) magnitude of $Y(t)$, and 3) magnitude of $V_y(t)$. Optimal synchronization between the vertical force and the heaving velocity, such that both are of the same sign for most of the cycle, is desired to avoid negative power occurrences. To achieve this good synchronization, well-timed LEVS appear to be necessary.

When the heaving velocity $V_y(t)$ is proportional to H_0 and f [see Eq. (2)], higher frequencies and/or higher heaving amplitudes appear favorable, whereas vertical force presents a complex dependency on both maximum effective angle of attack and maximum effective velocity.

It is clear that increasing the effective velocity [Eq. (4)] by increasing V_y (through H_0/c and/or f^*) leads to increased effective

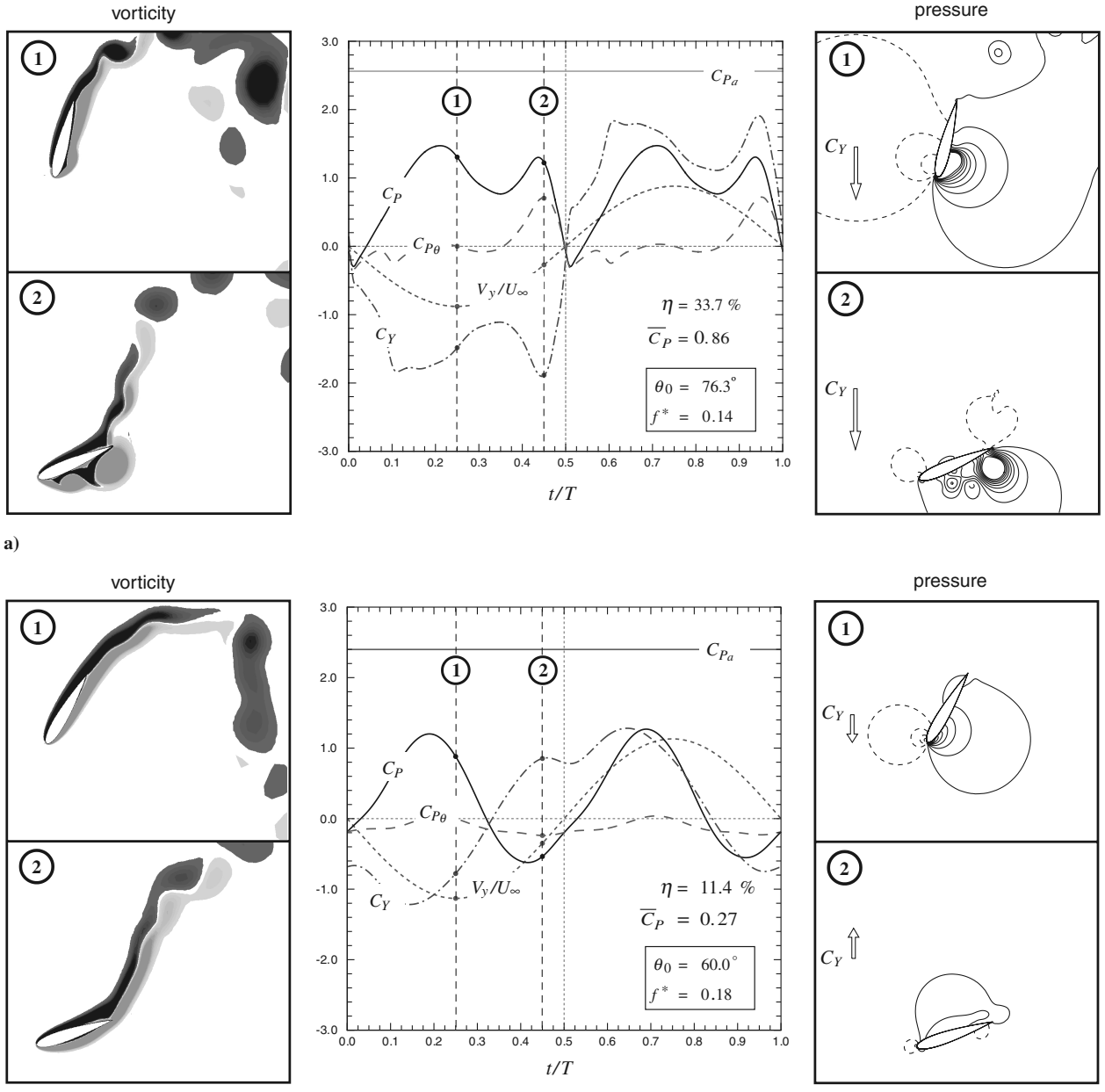

Fig. 12 Contours of vorticity (gray for positive ω and black for negative) and pressure (dashed for positive and solid for negative) at two instants in the cycle and the time evolution (center) of total power coefficient C_P, V_y/U_∞, C_Y, and C_{P_θ} for two power-extraction cases from Fig. 11: a) a typical high-efficiency case (case 1) in which the occurrence of LEVS implies optimal synchronization between Y vs V_y b) a moderate-efficiency case (case 2) in which no LEVS implies poor synchronization of Y vs V_y.

dynamic pressure and thus increased aerodynamic forces. However, the vertical force component Y may then decrease due to lower effective angle of attack and reduced vertical projection. Indeed, increasing either the frequency f or the heaving amplitude H_0 (everything else being the same) inevitably moves us toward the feathering limit, as shown in Fig. 13. This ultimately has a detrimental effect past a certain level. As observed in Fig. 11, an optimal efficiency in the (f^*, θ_0) parametric space must exist.

B. Parametric Study

The aerodynamics of oscillating airfoils is a rich and complex topic, due in part to its inherent unsteadiness, but also due to the number and wide ranges of its governing parameters, which are hereafter classified in three categories: motion, geometrical, and viscous parameters.

In the following sections, we consider the heaving amplitude H_0/c, the pitching amplitude θ_0, and the frequency f^* as motion parameters. These may be combined to give the maximum effective

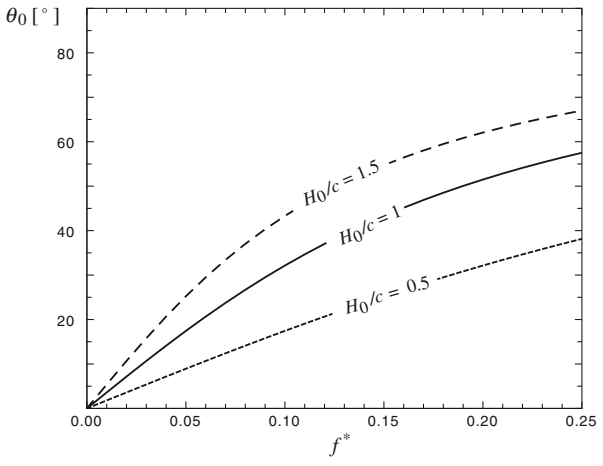

Fig. 13 Feathering curves in (f^*, θ_0) parametric space for different heaving amplitudes H_0/c.

Table 3 Effect of a larger heaving amplitude; NACA 0015; $x_p/c = 1/3$ and $Re = 1100$

	Case 1		Case 2	
	$f^* = 0.14$	$\theta_0 = 76.3$ deg	$f^* = 0.18$	$\theta_0 = 60.0$ deg
H_0/c	$\bar{C}_P$	η, %	$\bar{C}_P$	η, %
1.0	0.86	33.7	0.27	11.4
1.5	0.98	28.5	−0.69	−20.9

angle of attack reached in the airfoil cycle and the maximum effective velocity and dynamic pressure. The phase difference ϕ between heaving and pitching motions is also considered to be a motion parameter, but was not varied in this study. Note, however, that the constant value $\phi = 90$ deg used here was found to be nearly optimal for power extraction according to the pioneer experiments of McKinney and DeLaurier [1]. The airfoil geometric shape and the location of its pitching axis both fall in the geometry-related category, whereas the two viscous parameters considered here are the Reynolds number and, eventually, the effects of turbulence.

To gauge the impact and relative importance of the parameters that were held fixed up to this point (H_0, airfoil thickness, x_p, and Reynolds number), several extra simulations were computed, mainly for the two test cases illustrated in Fig. 12.

1. *Motion Parameters*

Through their direct effect on the airfoil inertia (translational and rotational accelerations), the motion parameters have an expectedly strong effect on flow dynamics. The overall impacts of the parameters f^* and θ_0 were addressed in the previous section. We now consider varying the heaving amplitude H_0 for a given (f^*, θ_0), which affects crucial characteristics such as the maximum angle of attack experienced by the airfoil [Eq. (5)] and its oscillating velocity [Eq. (2)]. Furthermore, changing H_0 also directly affects the size of the flow window swept by the airfoil (Fig. 1) and therefore the available power P_a through which one defines the efficiency.

Interestingly, we find that although efficiency η tends to decrease with an increase in heaving amplitude (Table 3), it does not necessarily imply that less power is extracted. Indeed, the data for case 1 in Table 3 show an increase in the mean power coefficient $\bar{C}_P$ but a decrease in efficiency when the heaving amplitude goes from 1 to 1.5 chords. This observation is particularly important to bear in mind when one is considering practical application of this turbine concept. One also notes that case 2 exhibits a negative power coefficient when $H_0/c = 1.5$, which can be explained by the fact that this parametric point now falls too close to its feathering limit (Fig. 13 with $H_0/c = 1.5$) to achieve a net power extraction in the mean.

In fact, the preceding observations suggest that the maximum effective angle of attack in the cycle (approximated by $|\alpha_{T/4}|$ here) might be a more appropriate characterizing parameter than the two separate amplitude parameters H_0 and θ_0. Indeed, the main flow characteristics (such as presence and timing of LEVS) are found to be very similar between cases exhibiting the same frequency and maximum effective angle of attack, but having quite different pitching and heaving amplitudes. This is clearly illustrated with the four cases shown in Fig. 14a, which span heaving amplitudes from 0 to 1.5 chords, but all share the same $f^* = 0.12$ and the same

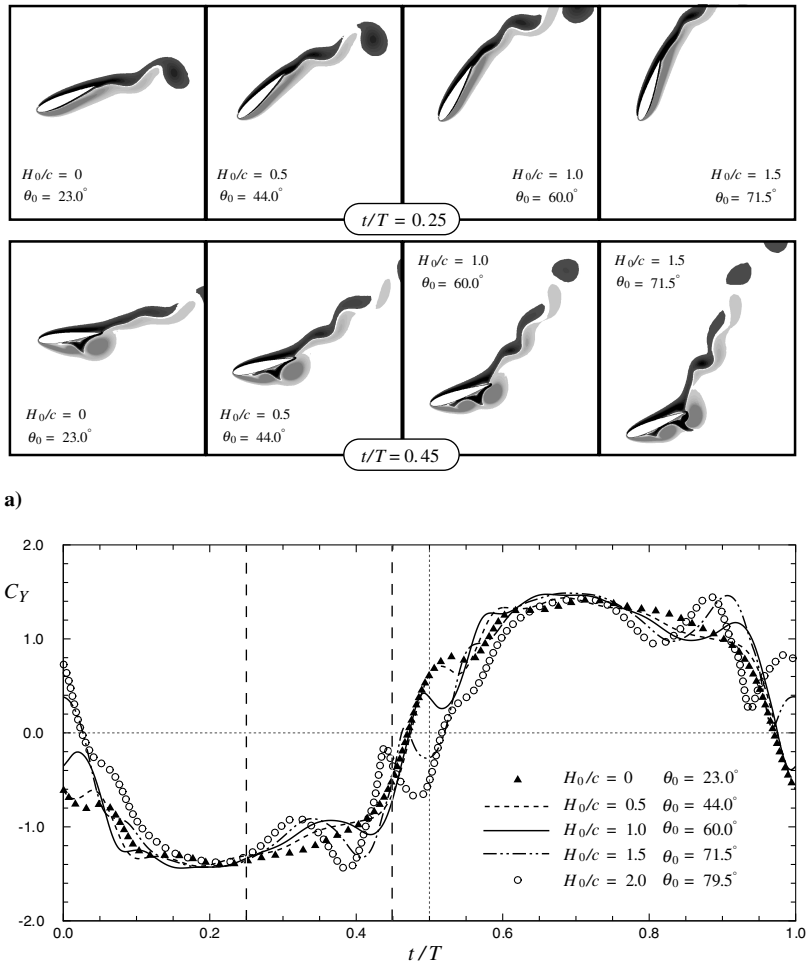

Fig. 14 Comparison of cases with the same frequency ($f^* = 0.12$) and a similar effective angle of attack ($|\alpha_{T/4}| = 23$ deg); NACA 0015; $x_p/c = 1/3$ and $Re = 1100$: a) vorticity fields (gray for positive ω and black for negative) at two different times and b) vertical force-coefficient evolutions over one periodic cycle.

Table 4 Comparison of cases at different H_0/c but same f^* and $\alpha_{T/4}$; NACA 0015; $x_p/c = 1/3$ and $Re = 1100$

f^*	$\lvert\alpha_{T/4}\rvert$, deg	θ_0, deg	H_0/c	$\bar{C}_P$	η, %
0.12	23.0	23.0	0.0	~0	0.8
0.12	23.3	44.0	0.5	0.29	20.8
0.12	23.0	60.0	1.0	0.59	24.5
0.12	23.0	71.5	1.5	0.89	26.3
0.12	23.0	79.45	2.0	1.13	25.8

Table 5 Effect of airfoil thickness; $H_0/c = 1$, $x_p/c = 1/3$, and $Re = 1100$

	Case 1		Case 2	
	$f^* = 0.14$	$\theta_0 = 76.3$ deg	$f^* = 0.18$	$\theta_0 = 60.0$ deg
NACA	$\bar{C}_P$	η, %	$\bar{C}_P$	η, %
0002	0.81	31.8	0.28	11.6
0015	0.86	33.7	0.27	11.4
0020	0.85	33.3	0.27	11.0

$|\alpha_{T/4}| = 23$ deg. Moreover, one observes for these cases that similarity in the occurrence and timing of LEVS has also led to concordant sign switch in the vertical force coefficient $C_Y(t)$ as well as to similar amplitudes over the periodic cycle, as corroborated by Fig. 14b. This latter observation is particularly surprising at first sight, considering the differences in effective dynamic pressure ($\frac{1}{2}\rho V_{\text{eff}}^2$) between the cases considered.

The vertical force-coefficient evolution thus appears to be primarily governed by the values of f^* and $\alpha_{T/4}$, at least in the range of interest in this study. The differences observed at closer inspection near $t/T = 0$ and $t/T = 0.5$ in Fig. 14b are likely due to differences in instantaneous pitching velocity, Ω being proportional to the pitching amplitude θ_0. Nonetheless, the general match between the C_Y curves presented is quite impressive and is found to hold even for the case with no heaving at all (only pitching, case $H_0/c = 0$).

Similarity of C_Y curves does not necessarily lead to similar performances. Values of mean power coefficient $\bar{C}_P$ and efficiency η for cases of Fig. 14 are reported in Table 4. Mean values of power extracted vary, because at constant frequency the heaving velocity amplitude depends on the heaving amplitude. An increase of the latter tends to increase the power extracted, because V_y increases and $P(t) \approx Y(t)V_y(t)$. However, because the total power available P_a also increases with H_0 (through a larger flow window), computed efficiencies η tend toward comparable values for cases with large enough heaving amplitudes. Note that the first case of Table 4, with no heaving amplitude at all (pitching only), shows a small power-extraction result through a net P_θ contribution [Eq. (9)].

2. *Geometry Parameters*

To gain some insight into the effect of airfoil thickness, simulations with two other symmetric airfoils were carried out keeping all other parameters the same. Airfoils with 2 and 20% relative thicknesses (NACA 0002 and NACA 0020) were selected for comparison with our basic airfoil. It was found that the impact on the level of extracted power (and therefore of efficiency) for our two test cases was rather weak, as shown in Table 5. Furthermore, for case 1, which exhibited LEVS when a NACA 0015 was considered, very little change in instantaneous forces is observed; one continues to obtain similar LEVS for all three airfoil thicknesses. However, a more significant change is noticed on the instantaneous forces in case 2. For the NACA 0015, one had occurrence of dynamic stall (separated boundary layer over most of the airfoil surface) but without rolling up of the shear layer and vortex shedding (Fig. 12b). This is also observed for the NACA 0020 airfoil, but not for the very thin NACA 0002. The smaller leading-edge radius of the NACA 0002 airfoil is seen to trigger LEVS (see Fig. 15a) with a partial reattachment at the trailing edge. Extrema in the resulting vertical

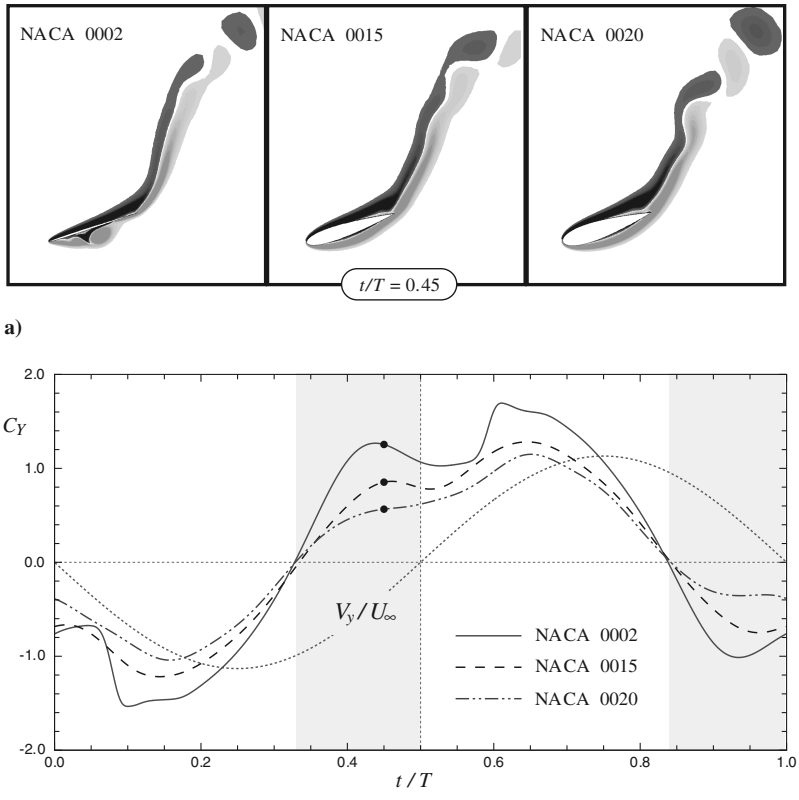

Fig. 15 Comparison of cases with different airfoil thicknesses; $Re = 1100$, $f^* = 0.18$, $\theta_0 = 60.0$ deg, $H_0/c = 1$, and $x_p/c = 1/3$: a) vorticity fields (gray for positive ω and black for negative) at $t/T = 0.45$ and b) vertical force-coefficient evolutions over one periodic cycle (shaded zones contribute negatively to power extraction).

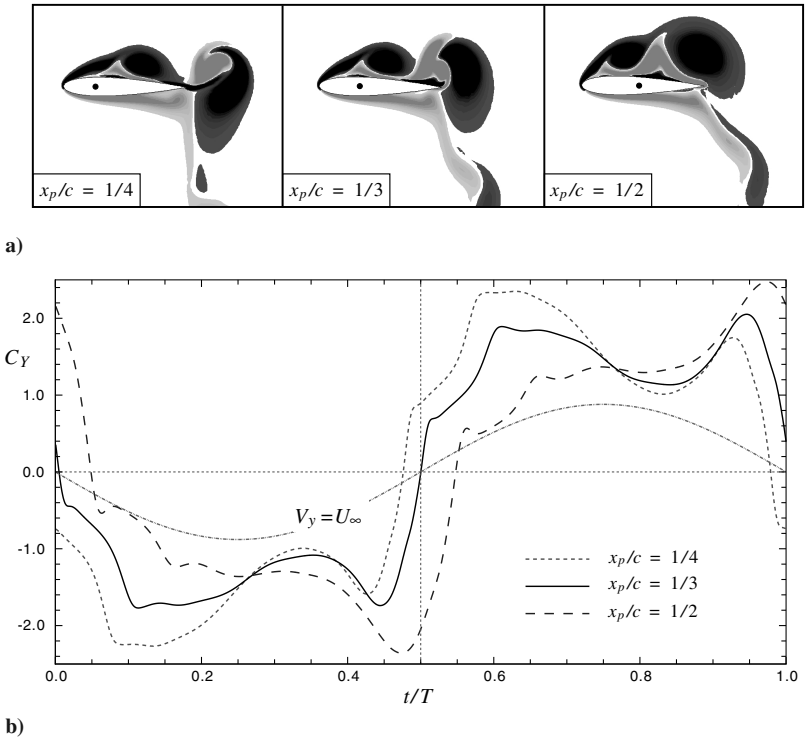

Fig. 16 Comparison of cases with different positions of the pitching center; NACA 0015; $Re = 1100$, $f^* = 0.14$, $\theta_0 = 76.3$ deg, and $H_0/c = 1$: a) vorticity fields (gray for positive ω and black for negative) at $t/T = 1$ and b) vertical force-coefficient evolutions over one periodic cycle.

force amplitude are thus increased, as shown in Fig. 15b. However, in the mean, the power extracted and the corresponding efficiency are quite similar for the three airfoils. We conclude here that efficiency is mostly insensitive to the details of the geometry, except for cases at the threshold of dynamic stall with no vortex shedding.

The preceding observations suggest that the aerodynamics at play here are very much inertial and are primarily governed by the forced large-amplitude oscillation. Although dynamic stall, and thus boundary-layer separation, was shown to play an important role in some cases, the precise location of flow separation along the airfoil is apparently not so critical for the cases considered here.

Let us now consider the second geometry parameter: namely, the location of the pitching axis. Changing the position of the pitching center along the chord of the airfoil directly modifies the instantaneous local acceleration of the body surface, leading to modified vorticity fluxes at the wall. This is an important aspect of these flows that is likely to alter the timing of vortex shedding for cases experiencing deep dynamic stall.

A comparison of our high-efficiency case (case 1) for three different pitching-center locations is shown in Fig. 16. From the instantaneous vorticity fields at $t/T = 1$, one sees that although vortex shedding occurs for each case, vortices will be shed earlier for a pitching center closer to the leading edge. Obviously, the timing of shedding may significantly affect the synchronization of vertical force and heaving velocity (sign switch). Indeed, for a pitching center at midchord, vortices are shed a bit late, resulting in a late sign switch of its vertical force coefficient relative to the heaving velocity (see Fig. 16b).

Table 6 Effect of pitching-center location; NACA 0015; $H_0/c = 1$ and $Re = 1100$

	Case 1		Case 2	
	$f^* = 0.14$	$\theta_0 = 76.3$ deg	$f^* = 0.18$	$\theta_0 = 60.0$ deg
x_p/c	$\bar{C}_P$	η, %	$\bar{C}_P$	η, %
1/4	0.89	33.1	0.23	9.3
1/3	0.86	33.7	0.27	11.4
1/2	0.69	29.4	0.24	10.7

Moreover, one notes that changing the pitching-center location has a deeper impact on force evolutions than does a mere time shift, because force amplitudes are also being affected. For practical reasons, we limited ourselves to pitching-axis locations from quarter- to midchord here. Nonetheless, 20% variations in resulting mean power coefficients and efficiencies are observed independently of the occurrence of vortex shedding, as presented in Table 6. Note that the total flow window swept by the airfoil is also slightly affected by the changes in x_p. The third-chord choice, $x_p/c = 1/3$, appears thus far to be a reasonable choice, from the present data.

Even though the pitching-center location does not appear in the expressions for pitching and heaving velocities [Eqs. (1) and (2)], its precise location has a direct influence on surface velocity distributions around the airfoil, thus profoundly affecting wall vorticity fluxes and boundary-layer states. Effects of pitching-axis location are therefore considered important, but still remain intricate.

3. *Viscosity Parameters*

Finally, the effect of viscosity was addressed in this investigation by simulating our two test cases with a smaller (500) and a larger (2400) Reynolds number, assuming laminar-flow conditions. We found that efficiency tends to increase slightly with Reynolds number, as shown in Table 7. Reduced viscous diffusion tends to yield thinner effective bodies and larger force coefficients, in good accordance with usual observations in stationary aerodynamics.

Table 7 Effect of Re number; NACA 0015; $H_0/c = 1$ and $x_p/c = 1/3$

	Case 1		Case 2	
	$f^* = 0.14$	$\theta_0 = 76.3$ deg	$f^* = 0.18$	$\theta_0 = 60.0$ deg
Re	$\bar{C}_P$	η, %	$\bar{C}_P$	η, %
500	0.84	32.7	0.24	9.8
1100	0.86	33.7	0.27	11.4
2400[a]	0.92	35.9	0.29	11.9
10,000[b]	0.93	36.4	0.32	13.5

[a]Mesh contains 79,000 cells.
[b]URANS Spalart–Allmaras model; mesh contains 154,000 cells.

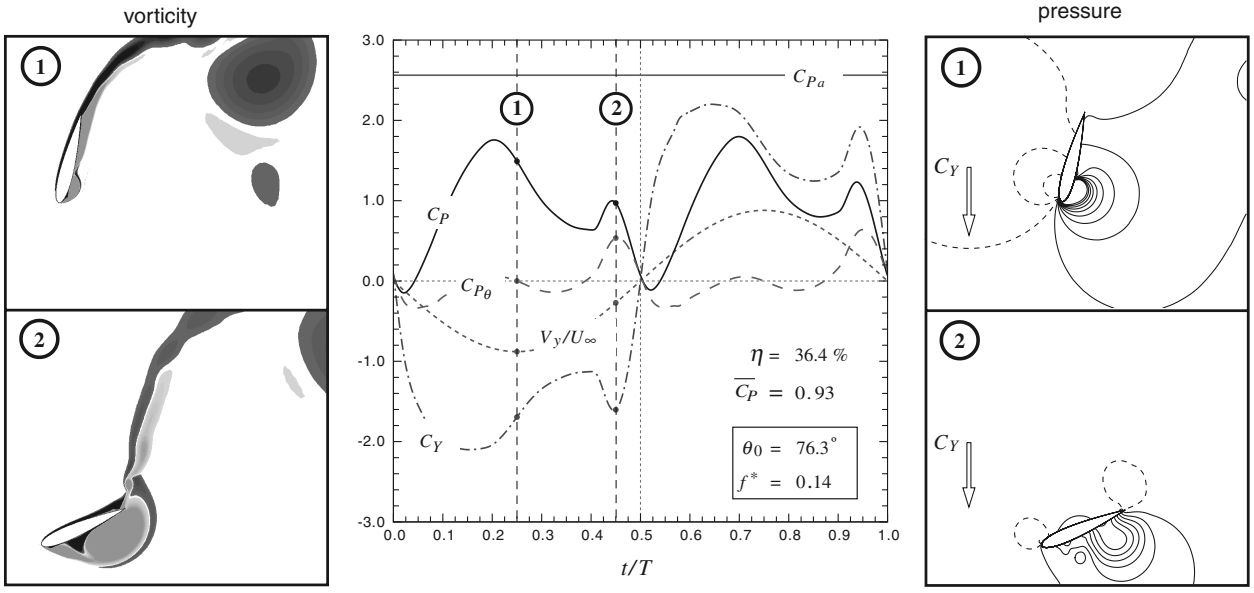

a)

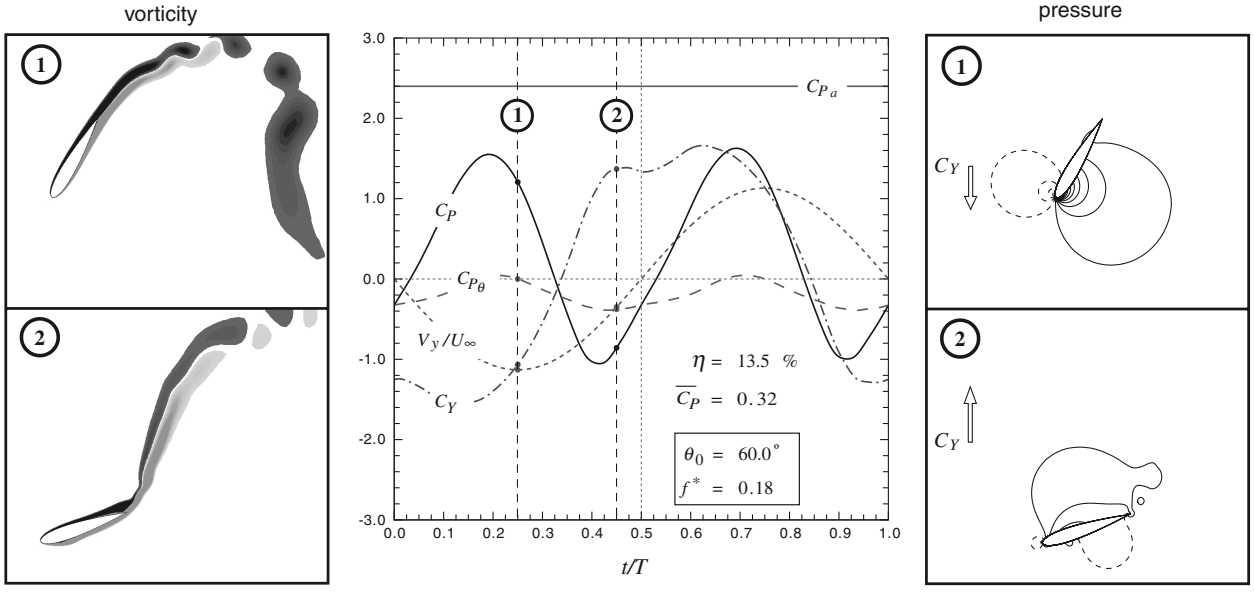

b)

Fig. 17 Contours of vorticity (gray for positive ω and black for negative) and pressure (dashed for positive and solid for negative) at two instants in the cycle and the time evolution (center) of total power coefficient C_P, V_y/U_∞, C_Y, and C_{P_θ} for a) test case 1 and b) test case 2 at $Re = 10,000$; URANS Spalart–Allmaras model; mesh contains 154,000 cells.

To get a preliminary glimpse into the effect of turbulence, we simulated our two test cases at a moderate Reynolds number of $Re = 10,000$ using the unsteady Reynolds-averaged Navier–Stokes (URANS) approach based on the Spalart–Allmaras model.

Because attached boundary layers are expected to remain laminar at that Reynolds number, it is mainly the effect of the turbulent diffusion in the near wake that is of interest here. Again, we find that efficiency tends to increase slightly for both cases (Table 7). Comparisons of Fig. 17 at $Re = 10,000$ with Fig. 12 at $Re = 1100$ indicate no major qualitative changes in the cycles of power extraction, except for slightly amplified extrema associated with amplified force coefficients. Attached boundary layers are indeed thinner at the higher Reynolds numbers, whereas separated vorticity layers and vortices are somewhat more diffused under the action of turbulent effective viscosity. In particular, the suction effect of the two shed vortices of case 1 in Fig. 12a is slightly reduced, due to the smearing and fusion of the shed vortices in the corresponding URANS simulation. For case 2, the pressure field suggests that boundary-layer reattachment is taking place somewhat earlier on the bottom surface of the airfoil, in which increased mixing is produced by turbulence generated in the so-called separation bubble.

V. Conclusions

The present investigation of the power-extraction potential of oscillating airfoils has shown that under laminar 2-D flow conditions, a single airfoil that is both pitching and heaving can reach efficiencies as high as about 35%. For a heaving amplitude of one chord, these high efficiencies are observed for reduced frequency $f^* \approx 0.15$ and high pitching amplitude $\theta_0 \approx 75$ deg. Under such conditions, maximum effective angles of attack in the cycles reach about 35 deg and dynamic stall occurs. It is shown that leading-edge vortex shedding is actually an important mechanism by which a good synchronization between the vertical force and the heaving velocity is achieved, thus yielding positive power extraction over most of the periodic cycle.

Our current parametric study has shown that the physics of such oscillating airfoils is mostly inertial, due to the large amplitude of the imposed motion. Motion parameters such as frequency, maximum effective angle of attack, and heaving amplitude primarily govern the predicted performances. Geometry parameters and viscous parameters do not have as much impact. The present results suggest that a pitching center at the third chord appears to be a reasonable choice and that airfoil performance in power extraction slightly increases with Reynolds number. Although the simulations performed in this study are two-dimensional and involve low-Reynolds-number flows, it is expected that the trends observed in this study and the relative impact of the parameters involved remain valid at higher Reynolds numbers, even though quantitative values may change due to thinner, more energetic, boundary layers and turbulence effects.

Future investigations should provide experimental measurements to help ascertain the impact of three-dimensionality and turbulence effects.

Acknowledgments

Financial support from Natural Sciences and Engineering Research Council of Canada is gratefully acknowledged. The authors would like to acknowledge colleagues from the Laboratoire de Mécanique des Fluides Numérique for fruitful discussions and, in particular, Steve Julien for manuscript revision and Julie Lefrançois and Pascal Bochud for their assistance with the Lagrangian simulations. The authors are also very grateful to G. S. Winckelmans from Université Catholique de Louvain in Belgium for providing the original vortex code used in this work.

References

[1] McKinney, W., and DeLaurier, J., "The Wingmill: An Oscillating-Wing Windmill," *Journal of Energy*, Vol. 5, No. 2, 1981, pp. 109–115.

[2] Jones, K. D., Lindsey, K., and Platzer, M. F., "An Investigation of the Fluid-Structure Interaction in an Oscillating-Wing Micro-Hydropower Generator," *Fluid Structure Interaction 2*, edited by Chakrabarti, Brebbia, Almorza, and Gonzalez-Palma, WIT Press, Southampton, England, U.K., 2003, pp. 73–82.

[3] Theodorsen, T., "General Theory of Aerodynamic Instability and the Mechanism of Flutter," NACA Rept. 496, 1935.

[4] Anderson, J. M., Streitlien, K., Barrett, D. S., and Triantafyllou, M. S., "Oscillating Foils of High Propulsive Efficiency," *Journal of Fluid Mechanics*, Vol. 360, Apr. 1998, pp. 41–72. doi:10.1017/S0022112097008392

[5] Betz, A., "Das Maximum der Theoretisch Möglichen Ausnützung des Windes Durch Windmotoren," *Zeitschrift für das Gesamte Turbinenwesen*, Vol. 26, Sept. 1920, pp. 307–309.

[6] FLUENT, Software Package, Ver. 6.1, ANSYS, Inc., Lebanon, NH, 2003.

[7] Ploumhans, P., and Winckelmans, G. S., "Vortex Methods for High-Resolution Simulations of Viscous Flow Past Bluff Bodies of General Geometry," *Journal of Computational Physics*, Vol. 165, No. 2, 2000, pp. 354–406. doi:10.1006/jcph.2000.6614

[8] Blackburn, H. M., and Henderson, R. D., "A Study of Two-Dimensional Flow Past an Oscillating Cylinder," *Journal of Fluid Mechanics*, Vol. 385, Apr. 1999, pp. 255–286. doi:10.1017/S0022112099004309

[9] Daeninck, G., Dumas, G., and Winckelmans, G., "Vortex Method for DNS About Arbitrarily Moving Multiple Bodies," 57th Annual Meeting of APS Division of Fluid Dynamics, American Physical Society, Paper BAPS04-AK.008, Nov. 2004.

K. Ghia
Associate Editor